Band-Mott mixing hybridizes the gap in $Fe_2Mo_3O_8$

K. Park,[1,*] G. L. Pascut,[2,*] G. Khanal,[3] M. O. Yokosuk,[1] Xianghan Xu,[3] Bin Gao,[4] M. J. Gutmann,[5] A. P. Litvinchuk,[6] V. Kiryukhin,[3,7] S. -W. Cheong,[3,7,8] D. Vanderbilt,[3] K. Haule,[3] and J. L. Musfeldt[1,9,†]

[1]*Department of Chemistry, University of Tennessee, Knoxville, Tennessee 37996, USA*
[2]*MANSiD Research Center and Faculty of Forestry, Applied Ecology Laboratory, Stefan Cel Mare University (USV), 13 University Road, Suceava 720229, Romania*
[3]*Department of Physics and Astronomy, Rutgers University, Piscataway, New Jersey 08854, USA*
[4]*Department of Physics and Astronomy, Rice University, Houston, Texas 77005, USA*
[5]*ISIS Facility, STFC-Rutherford Appleton Laboratory, Didcot OX11 OQX, United Kingdom*
[6]*Texas Center for Superconductivity and Department of Physics, University of Houston, Houston, Texas 77204, USA*
[7]*Rutgers Center for Emergent Materials, Rutgers University, Piscataway, New Jersey 08854, USA*
[8]*Laboratory for Pohang Emergent Materials and Max Planck POSTECH Center for Complex Phase Materials, Pohang University of Science and Technology, Pohang 790-784, Korea*
[9]*Department of Physics and Astronomy, University of Tennessee, Knoxville, Tennessee 37996, USA*

(Received 5 November 2020; revised 2 November 2021; accepted 4 November 2021; published 22 November 2021)

We combined optical spectroscopy and first-principles electronic structure calculations to reveal the charge gap in the polar magnet $Fe_2Mo_3O_8$. Iron occupation on the octahedral site draws the gap strongly downward compared to the Zn parent compound, and subsequent occupation of the tetrahedral site creates a narrow resonance near the Fermi energy that draws the gap downward even further. This resonance is a many-body effect that emanates from the flat valence band in a Mott-like state due to screening of the local moment—similar to expectations for a Zhang-Rice singlet, except that here it appears in a semiconductor. We discuss the unusual hybridization in terms of orbital occupation and character as well as the structure-property relationships that can be unveiled in various metal-substituted systems (Ni, Mn, Co, Zn).

DOI: 10.1103/PhysRevB.104.195143

I. INTRODUCTION

3*d*-containing materials are well known for strong electron correlations, narrow bandwidths, site- and orbital-selective states, and robust magnetism, whereas 4*d* and 5*d* systems are recognized for strong spin-orbit coupling, increased hybridization, extended orbitals, and a tendency toward dimerization [1]. Combining these qualities in mixed metal materials leads to a variety of unexpected properties. Examples include interpenetrating sublattices with independent spin dynamics and ground states in Sr_2CoOsO_6 [2,3], self-healing photoelectrode materials such as $CuRhO_2$ [4], covalency-driven collapse of spin-orbit coupling in $Ba_5CuIr_3O_{12}$ [5], an ultrahigh coercive field in Sr_3NiIrO_6 [6,7], magnetoelectric coupling in $Co_4Nb_2O_9$ [8], surprising spin entropy effects across the magnetic quantum phase transition in $CoNb_2O_6$ [9], and nonreciprocal directional dichroism in Ni_3TeO_6 [10]. Another mixed metal system with exciting properties and curious hybridization is $Fe_2Mo_3O_8$—also known as the mineral kamiokite [11]. While magnetism and magnetoelectric coupling have been widely studied [12–19], the charge excitations are highly underexplored.

$Fe_2Mo_3O_8$ is a polar magnet with giant magnetoelectric coupling, strong Dzyaloshinski-Moriya interactions, valence bond condensation (creating a cluster magnet), and the possibility of orbitally selective transitions [12–19]. Zinc substitution, first on the tetrahedral Fe site and then on the octahedral Fe site [15,20], is of interest for magnetic properties as well [11,13,20,21]. The structure of $Fe_2Mo_3O_8$ consists of corner-shared tetrahedral and octahedral sites separated by layers of Mo trimers [Figs. 1(a) and 1(b)] [12,22,23]. The FeO_4 tetrahedron is significantly elongated and distorted, and the FeO_6 octahedron is trigonally distorted as well, leading to a C_{3v} point group on both the tetrahedral and octahedral Fe sites. As a result, $Fe_2Mo_3O_8$ has no inversion symmetry. The system has a 61 K magnetic ordering transition to a collinear antiferromagnetic state with a concomitant structural distortion [14,24–27]. Antiferromagnetic antiphase domain boundaries have been imaged in this state [28]. $Fe_2Mo_3O_8$ also displays a 5 T transition to the ferrimagnetic state with an extremely large magnetoelectric coefficient [14,15]. $Ni_2Mo_3O_8$ also hosts robust magnetoelectric coupling with a field-tunable coupling mechanism [29]. Spectroscopic highlights in $Fe_2Mo_3O_8$ include (i) nonreciprocal directional dichroism [30], phonon trends across T_N [26,27], and a variety of magnetic excitations in the terahertz range [31], (ii) Mössbauer to confirm the 2+ charge on the iron site [24,25], and (iii) studies of charge transfer via time-dependent optical Kerr effects [32] complemented by first-principles electronic structure calculations [20,27,33].

In order to place the charge excitations on a firm foundation, we measured the optical properties of the $A_2Mo_3O_8$

*These authors contributed equally to this work.
†musfeldt@utk.edu

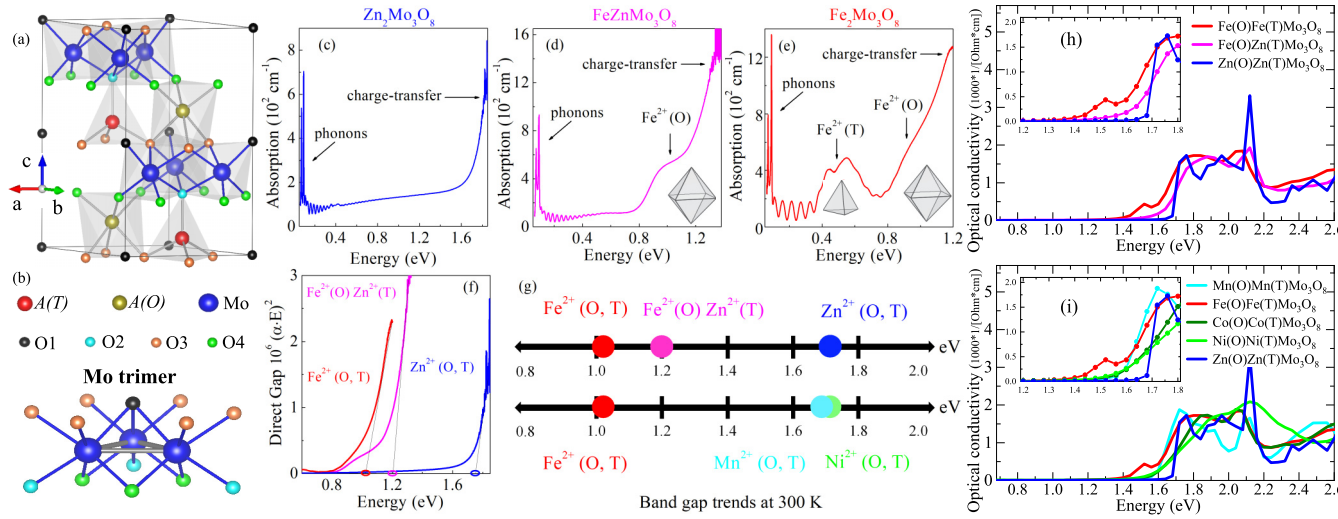

FIG. 1. (a) Crystal structure of the $A_2Mo_3O_8$ compounds where A = Mn, Fe, Co, Ni, Zn. A(T) and A(O) represent ions in trigonally distorted tetrahedral and octahedral environments, respectively. (b) Schematic view of the Mo trimer. (c)–(e) Absorption spectra of $Zn_2Mo_3O_8$, $FeZnMo_3O_8$, and $Fe_2Mo_3O_8$ measured at room temperature. (f) A Tauc plot reveals the direct band gap of $Zn_2Mo_3O_8$ and the Fe-substituted analogs. (g) Band-gap schematic showing the impact of two different types of T- and O-site substitution. The upper and lower trend lines correspond to the $(Fe,Zn)_2Mo_3O_8$ series and the $A_2Mo_3O_8$ (A = Fe, Mn, Ni) materials, respectively. (h), (i) Calculated optical conductivity of the $A_2Mo_3O_8$ materials.

family of materials (where A = Fe, Ni, Mn, Zn) and compared our findings with complementary electronic structure calculations. We show that the 1.7 eV gap in $Zn_2Mo_3O_8$ is determined by the charge excitations of the Mo trimer. Replacing Zn on the octahedral site with Fe yields $FeZnMo_3O_8$. This system has a substantially reduced and renormalized gap determined by Fe-O hybridized bands that appear due to the periodic lattice potential. Further substitution yields $Fe_2Mo_3O_8$, which has both trigonally distorted octahedral and tetrahedral sites occupied by Fe atoms, and the gap is reduced to 1.0 eV. Here, the charge gap is more complex to describe because it has mixed band and Mott features. In other words, some orbitals hybridize strongly with oxygen and form very narrow bands, whereas other orbitals exhibit real-space localization and are Mott insulating. Mixed band and Mott gaps are commonly called orbitally or site-selective Mott states [34–39]. What distinguishes $Fe_2Mo_3O_8$ from other orbitally selective Mott systems is the narrow many-body resonance emanating from the edge of the flat valence band. The Kondo effect is, of course, normally studied in metals. In this work, we show that the Kondo effect can also appear in mixed metal semiconductors. In addition, the gap in $Fe_2Mo_3O_8$ is sensitive to magnetic ordering at 61 K due to the heavily mixed character of the charge excitations. Moreover, the d-to-d excitations on the distorted octahedral Fe site are vibronically activated, and spin-orbit related features ride on top of the distorted tetrahedral on-site excitations below the magnetic ordering transition. We discuss these findings in terms of band-Mott mixing in $3d$- and $4d$-containing quantum cluster magnets.

II. METHODS

High-quality single crystals of $Fe_2Mo_3O_8$, the Zn-substituted analogs $FeZnMo_3O_8$, and $Zn_2Mo_3O_8$, as well as $Mn_2Mo_3O_8$ and $Ni_2Mo_3O_8$ were grown by chemical vapor transport, as discussed previously [14]. Special care was taken to assure the stoichiometry of $FeZnMo_3O_8$. Crystals were polished to control optical density and expose the hexagonal face. A Bruker 55 Fourier transform infrared spectrometer equipped with a microscope attachment was used to measure transmittance over the 0.41–2.0 eV energy range. Absorption was calculated as $\alpha(E) = -\frac{1}{d}\ln[\mathcal{T}(E)]$, where $\mathcal{T}(E)$ is the transmittance and d is the thickness. Performing these measurements in transmittance rather than reflectance avoids light leakage problems. Temperature was controlled by an open-flow cryostat.

For theoretical calculations, we used the density functional theory (DFT) as implemented in WIEN2K [40] and a charge-self-consistent dynamical mean-field theory (DMFT) as implemented in the EDMFT code [41,42]. At the DFT level, we used the generalized gradient approximation Perdew-Burke-Ernzerhof (GGA-PBE) functional [43], with RKmax = 7.0 and 312 k points in the irreducible part of the first Brillouin zone. At the eDMFT level, we used the fully rotationally invariant Coulomb interaction, a nominal double-counting scheme [44], with the d-orbital occupations for double-counting corrections for Mn, Fe, Co, and Ni set to be 5, 6, 7, and 8, respectively. The temperature is fixed at 500 K. To define the DMFT projector, we used quasiatomic orbitals by projecting bands in a large hybridization window (−10 to +10 eV) with respect to the Fermi level, in which partially screened Coulomb interactions have values of $U = 10$ eV and $J_H = 1$ eV in Mn, Fe, Co, and Ni ions. In order to solve the auxiliary quantum impurity problem, a continuous-time quantum Monte Carlo method in the hybridization expansion (CT-HYB) was used [45], where the five d orbitals for the Mn, Fe, Co, and Ni ions (grouped according to the local C_{3v} point group symmetry) were chosen as our correlated subspace in a single-site DMFT approximation. For the CT-HYB calculations, up to 10^8 Monte Carlo steps were employed for

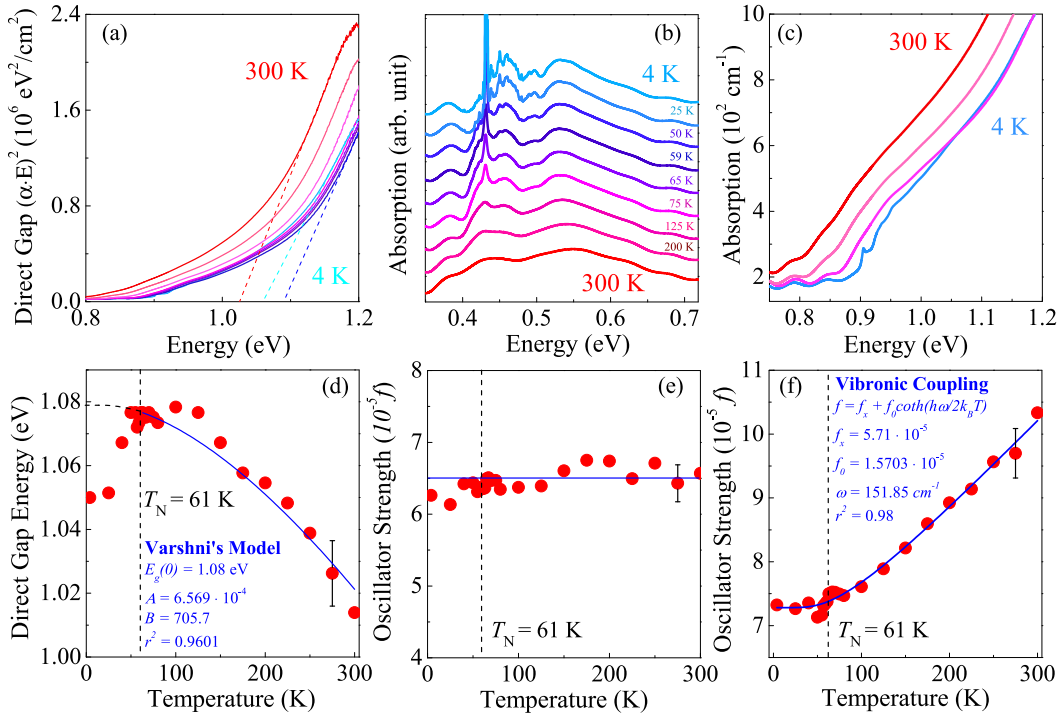

FIG. 2. (a),(d) Tauc plot of $(\alpha E)^2$ vs energy for $Fe_2Mo_3O_8$ and band gap vs temperature with a fit to the Varshni model. (b),(e) Close-up view of the Fe^{2+} d-to-d on-site excitation on the tetrahedral site showing the fine structure that develops due to spin-orbit coupling below the 61 K magnetic ordering transition. (c),(f) Close-up view of the Fe^{2+} d-to-d on-site excitation on the octahedral site and oscillator strength vs temperature along with a fit to a modified vibronic coupling model [49–51].

each Monte Carlo run. The self-energy on the real axis was obtained using the analytical continuation maximum entropy method for the local cumulant, as explained in [46]. During the calculation, the position of the chemical potential was kept fixed within the gap. The experimental crystal structures used for our computations [26] as well as details of our calculations are given in the Supplemental Material [47].

III. RESULTS AND DISCUSSION

A. Optical response of $Fe_2Mo_3O_8$ and the A-substituted analogs (A = Zn, Mn, Ni)

Figures 1(c) and 1(e) summarize the optical properties of the (Fe,Zn)Mo_3O_8 family of materials. The absorption spectrum of the parent compound, $Zn_2Mo_3O_8$, is low and flat in the near infrared, rising on approach to the O $2p$ → Mo $3d$ charge transfer excitation. The direct band gap is 1.75 eV. Because Zn^{2+} has a d^{10} configuration, there are no d-to-d on-site excitations. $Zn_2Mo_3O_8$ therefore provides an opportunity to study how the Mo trimer interacts with oxygen in isolation. At the same time, it is an important scaffold upon which additional complexity can be built.

Sequential A-site substitution of Fe, first into the distorted octahedral site in $FeZnMo_3O_8$, here denoted as Fe(O), and then into the distorted tetrahedral site in $Fe_2Mo_3O_8$, henceforth Fe(T), lowers the charge gap significantly [Fig. 1(f)]. We find direct gaps of 1.2 and 1.0 eV for $FeZnMo_3O_8$ and $Fe_2Mo_3O_8$, respectively. The gap values were determined from Tauc plots of $(\alpha E)^2$ vs energy [48].

Figure 1(d) displays the absorption of $FeZnMo_3O_8$. The charge excitations across the gap consist of mixed O $2p$ + Mo $3d$ + Fe(O) $3d$ transitions. The lowest-energy excitation across this gap comes from Fe(O) hybridizing with Mo-O trimers. The 1.2 eV gap is substantially lower in energy than the fundamental Mo-O band gap, which theoretically remains roughly equal to that in $Zn_2Mo_3O_8$. As Fe^{2+} populates the octahedral site in $FeZnMo_3O_8$, an on-site d-to-d transition arises near 0.95 eV. It overlaps strongly with the leading edge of the charge transfer band and is activated by vibronic coupling [Figs. 2(c) and 2(f)] [49–51]. Notice that absorption is low and flat near 0.5 eV—a sign of crystal quality and stoichiometry. Once the Fe(T) site is populated as well (as in $Fe_2Mo_3O_8$), the gap is reduced further, and two different types of d-to-d on-site excitations are identified inside the charge gap. As shown in Fig. 1(e), Fe on the trigonally distorted tetrahedral site contributes additional atomic-line excitations centered at 0.5 eV. While oscillator strength is fully conserved as a function of temperature [Fig. 2(e)], a great deal of fine structure due to spin-orbit coupling rides on top of the band below the 61 K magnetic ordering transition [Fig. 2(b)]. A similar response develops in Fe^{2+}:ZnSe [52]. The behavior of the Fe^{2+} on-site d-to-d excitations in $Fe_2Mo_3O_8$ is summarized in Figs. 2(b), 2(c), 2(e), and 2(f) and further discussed in the Supplemental Material [47]. The full sequence of gap values is shown schematically in Fig. 1(g).

To test the influence of A-site substitution on the band gap and strength of the metal to MoO-trimer hybridization, we measured the optical properties of the Mn and Ni analogs of $Fe_2Mo_3O_8$ (Fig. S2, Supplemental Material [47]). $Mn_2Mo_3O_8$ and $Ni_2Mo_3O_8$ have charge gaps of 1.65 and 1.7 eV, respectively—very similar to that of the Zn end member. This result is attributable to $3d$ orbital filling and

character. The Mn system has a half-filled d manifold, which corresponds to a high spin Mott state with a large gap. The d^8 configuration in the Ni analog also has two holes and is thus in the large gap Mott insulating state. As a result, there is little mixing between the metal center and Mo-O trimer, and hence these transition metals do not play an active role in determining the low-energy excitations across the gap. We mention in passing that the Mn and Ni compounds have on-site d-to-d excitations as well (Fig. S2, Supplemental Material [47]).

On the other hand, $Fe_2Mo_3O_8$ has both Mott-type and band-insulating orbitals, which strongly hybridize with the Mo trimer. These interactions enable the Fe centers to control the low-energy physics as discussed below. Moreover, we find that the band gap of $Fe_2Mo_3O_8$ is sensitive to the 61 K magnetic ordering transition and the associated structural distortion [Figs. 2(a) and 2(d)]. This is different from the other $A_2Mo_3O_8$ compounds, where the temperature dependence of the band gaps is in excellent overall agreement with the Varshni model [53,54], implying no (or extremely subtle) structural aspects to the magnetic ordering transitions. That the band gap decreases across T_N is due to coupling of charge, structure, and magnetism and the flat bands emanating from the trigonally distorted tetrahedral Fe site.

B. Strong hybridization, resonance, and interaction with the Mo trimer

Figure 1(h) displays the theoretical optical conductivity of $Zn_2Mo_3O_8$, $FeZnMo_3O_8$, and $Fe_2Mo_3O_8$ computed using a combination of density functional theory and embedded dynamical mean-field theory (DFT + eDFMT) methods [41,42]. Here, we find the same trend of decreasing charge gap with Fe substitution. In $Zn_2Mo_3O_8$, the size of the optical gap is $\approx$1.7 eV, which decreases to approximately 1.5 and 1.4 eV in $FeZnMo_3O_8$ and $Fe_2Mo_3O_8$, respectively. Figure 1(i) compares the theoretical optical conductivity of the Mn, Ni, and Co analogs. We find that the predicted gap is larger in all of these compounds (near 1.55 eV) as compared to $Fe_2Mo_3O_8$. The edge of the gap is very smooth and temperature smeared. This is quite different from $Fe_2Mo_3O_8$, where the gap is smaller with an additional peak at the onset.

To better understand what determines the low-energy excitations and character of the gap in this class of compounds, we calculated the local density of states for the full set of $A_2Mo_3O_8$ materials [Fig. 3]. While the optical gap in general is different than the gap of the single-particle excitations measured by the local density of states, the two are very similar in these compounds. This is because the band gap is direct in $Zn_2Mo_3O_8$, and the hybridized bands in the Fe-containing compounds are extremely narrow. Hence momentum-conserving excitations have essentially the same gap size as the finite momentum single-particle excitations. The insets show that the position of the conduction band in $FeZnMo_3O_8$ and $Fe_2Mo_3O_8$ decreases slightly as compared to $Zn_2Mo_3O_8$, although the change is small. Most of the action is in the valence bands, where the FeZn band edge moves considerably upward. In $Fe_2Mo_3O_8$, a very narrow many-body excitation forms at the onset of the gap. This is the origin of the first peak in the optical conductivity [Figs. 1(h) and 1(i)] and the reason that the gap is drawn strongly downward in this system.

Figures 3(b)–3(g) display the projected density of states (DOS) per transition metal center and per orbital in the distorted tetrahedral (T) and octahedral (O) environments. The local point group symmetry around each iron center is C_{3v}. Therefore, the e and t_2 levels at the distorted tetrahedral site break into $e(1)$, a_1, and $e(2)$ orbitals. Similarly, symmetry at the trigonally distorted Fe octahedral site breaks t_{2g} and e_g into $e(2)$, a_1, and $e(1)$ states. These energy levels are shown in Fig. 4, and the symmetry breaking is diagrammed in Fig. S1 of the Supplemental Material [47].

Regarding Figs. 3(b)–3(g), we notice that the Mo states (dotted gray line) are very similar across this entire family of materials. The low-energy excitations are, however, not on the Mo site when Fe is present. Figure 3(b) reveals that the sharp many-body resonance near -0.4 eV emanates primarily from the Fe center in the trigonally distorted tetrahedral environment, $e(1)$. Figure 3(c) shows that a broader, but still reasonably sharp excitation around -0.8 eV arises from the doubly degenerate $e(2)$ state on the distorted octahedral site. Since both of these fairly sharp excitations come from band formation via hybridization, the Mo partial density of states also has a small peak at the same energy (Figs. S19 and S20 of the Supplemental Material [47]). This demonstrates the quasiparticle nature of these peaks, which are Kondo-like and come from local spin screening on the aforementioned $e(1)$ and $e(2)$ distorted tetrahedral and octahedral orbitals, respectively.

What is exciting about this finding is that screening and many-body Kondo peak formation [55,56] are normally expected in a metal—not an insulator. The possibility of a Kondo resonance in a semiconductor such as $Fe_2Mo_3O_8$ is potentially quite interesting, opening the door to deeper exploration of the Kondo effect in a significantly wider variety of materials. While broader peaks such as that at -0.8 eV are not uncommon in transition metal compounds and appear, for example, in monoxides [57,58], the very narrow resonance emanating from the $e(1)$ orbitals on the distorted tetrahedral site is unique to $Fe_2Mo_3O_8$. We assign it as an analog of the Zhang-Rice singlet in cuprates, [59,60] arising due to screening of the spin-1/2 hole on the trigonally distorted tetrahedral Fe $e(1)$ sites in the Mott insulating state. This characteristic peak appears with very well-defined energy. It also mixes strongly with the Mo-O trimers (see Supplemental Material, Fig. S5 [47]).

In order to test these predictions, we compare the theoretical optical conductivity [Fig. 1(h)] to the measured absorption spectrum of $Fe_2Mo_3O_8$ [Fig. 1(f)]. Overall, the calculated optical conductivity and the measured absorption spectrum are very consistent—although the features are not as well defined as we might prefer. As a reminder, the spectral functions are very flat on the valence edge due to Fe occupation on the distorted tetrahedral site. This causes a sharp many-body resonance in the density of states [Fig. 3(b)], which manifests as a small peak on the leading edge of the theoretical optical conductivity. The contribution from the distorted octahedral site is similar but less pronounced. Our calculations therefore predict that the many-body resonance on the valence band edge [Figs. 3(b) and 3(c)] should lower the gap. This is exactly what we find. Obviously, this structure is strongly

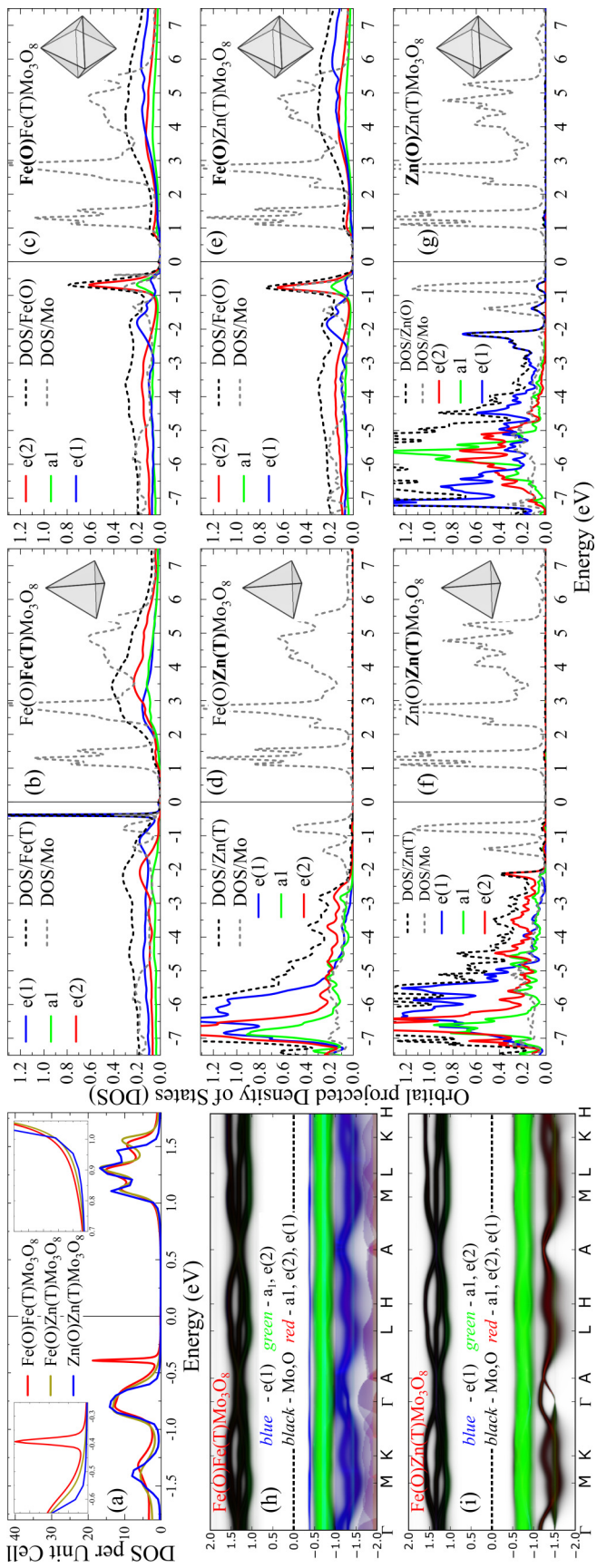

FIG. 3. Density of states (DOS) for $A_2Mo_3O_8$ (A = Fe and Zn): (a) total DOS, (b)–(g) atom- and orbital-projected DOS. The (T) and (O) symbols refer to trigonally distorted tetrahedral and octahedral environments. The vertical solid lines are placed at zero chemical potential. The schematic insets of gray tetrahedra/octahedra are guides to the eye, pointing the reader to the electronic states of the transition metal ions in the corresponding environment. (h), (i) Orbital projected spectral functions for $Fe_2Mo_3O_8$ and $FeZnMo_3O_8$ [blue: $e(1)$ tetrahedra; green: a_1 and $e(2)$ octahedra; red: a_1, $e(2)$ tetrahedra and $e(1)$ octahedra].

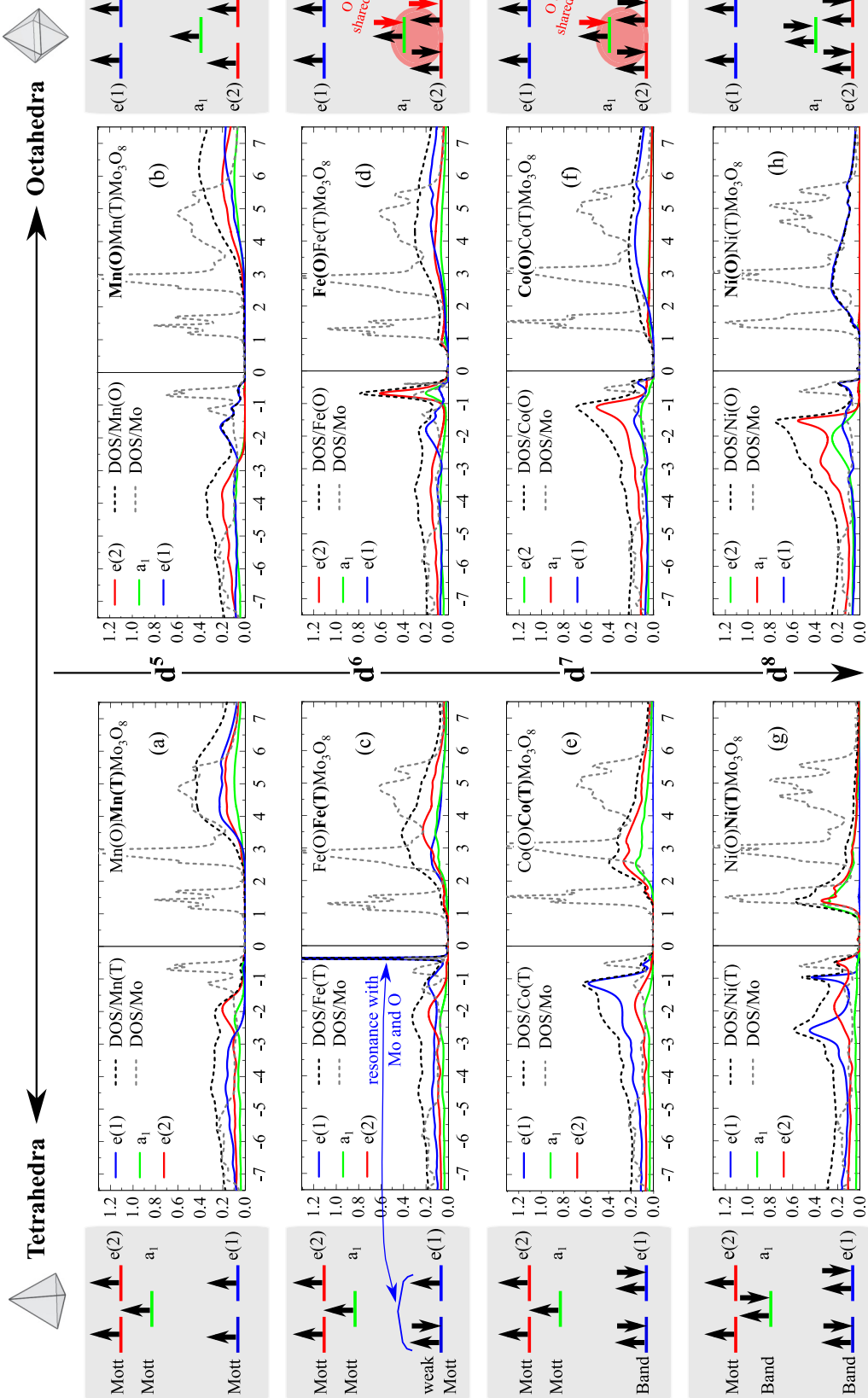

FIG. 4. Atom- and orbital-projected density of states (DOS) together with a schematic view of the orbital occupation and character for $A_2Mo_3O_8$ (A = Mn, Fe, Co and Zn). Each panel shows a schematic view of the orbital occupation (left side) and DOS (right side). (a),(c),(e),(g) Ions in trigonally distorted tetrahedral environments [A(T)]; (b),(d),(f),(h) Ions in trigonally distorted octahedral environments [A(O)].

broadened in the experimental result, but the presence of these states causes the gap to be drawn noticeably downward in this system [Fig. 1(f)]. Similar reasoning applies to $FeZnMo_3O_8$, although only the distorted octahedral site is operative. Because the density of states are momentum averaged, we also show the spectral functions [Figs. 3(h) and 3(i)].

C. Structure-property relations in the metal-substituted analogs

Figure 4 compares the density of states in $Fe_2Mo_3O_8$ with several other transition metal analogs which have orbital filling between d^5 and d^8—namely, the Mn, Co, and Ni analogs. We also show a schematic view of the orbital occupation for both the distorted tetrahedral and octahedral sites (left and right columns, respectively). The gap in each orbital can originate from the band structure due to the periodic potential (band gap) or from Mott localization of electrons on a given *A* site, which we denote as a Mott gap. In principle, we can distinguish between the two because the single-particle spectral function is modified from the DFT bands by self-energy effects. We expect the spectral function to be either zero or finite in the band-gap case; it should diverge inside the gap for the Mott case [61–63]. Here, the electron state can no longer be described within the band picture.

The top panels of Fig. 4 show calculations for $Mn_2Mo_3O_8$ in which the electrons are in the high-spin d^5 configuration. The Mott gap opens in all orbitals on both tetrahedral and octahedra sites, and it is much larger than the band gap of the Mo trimer. Consequently, the charge gap and low-energy excitations in the Mn and Zn compounds are determined by the same Mo-trimer states. This is why they appear so similar.

$Fe_2Mo_3O_8$ is the most interesting of the series, showing a complex interplay of band gaps, Mott gaps, and quasiparticle multiplets. The a_1 and $e(2)$ states on the distorted tetrahedra are Mott insulating with a large gap. As discussed above, the doubly degenerate $e(1)$ orbitals contain one hole, which is equally distributed among the two orbitals, and the Mott mechanism opens the gap—even though the self-energy pole is less strong and the gap is smaller than in the a_1 and $e(2)$ states. Moreover, at the edge of the gap, strong hybridization, directly computable by the DMFT hybridization function, shows a very strong and narrow peak due to many-body screening effects. With this mechanism, the spin-1/2 emanating from the $e(1)$ orbitals on the tetrahedral site is screened by the Mo-trimer electrons—a mechanism that is analogous to the Zhang-Rice state in cuprates [59]. Note that this is different from the sharp peak due to the valence band edge in transition metal monoxides [57,58]. The latter appears in the antiferromagnetic state where all gaps are bandlike in nature and spin states are split by a Zeeman field. As a consequence, many-body screening of the spin is not possible. Here, spin preserves SU(2) symmetry, and the resonance screens the local spin on Fe. In addition, the narrow peak due to many-body screening effects disappears in the antiferromagnetic ground state (Fig. S19, Supplemental Material [47]). The distorted octahedral site in the Fe d^6 state contains a combination of a Mott gap in the $e(1)$ states and a band gap in the a_1 and $e(2)$ states. This unusual combination is a so-called orbitally selective Mott state [37,38]. Note that the sharp peak at the valence band edge appears as well, even though it is not as sharp as the resonance from the distorted tetrahedral Fe $e(1)$ site. Its nature is different, as it appears in band-insulating a_1 and $e(2)$ orbitals similar to the valence band edge discussed in transition metal monoxides [57,58]. Hybridization and band formation with oxygen and Mo electrons are needed to open the band gap in the octahedral Fe a_1 and $e(2)$ states. This is because the latter contains only four electrons in three nearly degenerate a_1 and $e(2)$ orbitals.

Next we discuss the Co analog, which is in the d^7 configuration. In this case, the $e(1)$ orbitals on the tetrahedral site are fully filled, and the a_1 and $e(2)$ orbitals are in the high-spin Mott insulating state with a large gap—larger than the Mo-trimer gap. On the octahedral site, the $e(1)$ orbitals are Mott insulating with a large gap, and the a_1 and $e(2)$ states are band insulating, in which Mo and oxygen provide one electron to form a covalent band with the a_1 electrons. We note that no sharp low-energy peak is found at the valence band edge, although in principle such a peak is possible.

Figures 4(g) and 4(h) display the partial density of states for the Ni analog with its d^8 configuration. In this case, the $e(1)$ and a_1 orbitals on the distorted tetrahedral site are fully filled, and the doubly degenerate $e(2)$ state shows a Mott gap which is comparable to that of the Mo trimer. On the distorted octahedral site, the $e(2)$ and a_1 states are fully filled, and the $e(1)$ states are in the half-filled Mott insulating state. This Mott gap is again comparable to the Mo-trimer gap. Hence the reduction of the gap as compared to the Zn analog is minimal.

IV. SUMMARY AND OUTLOOK

To summarize, we measured the optical properties of $Fe_2Mo_3O_8$ and compared our findings with first-principles electronic structure calculations. We find a 1.1 eV direct gap composed of heavily mixed, charge transfer excitations that is sensitive to magnetic ordering at 61 K, vibronic coupling that activates on-site *d*-to-*d* excitations on the distorted octahedral Fe site, and spin-orbit related features riding on top of the *d*-to-*d* excitation on the distorted tetrahedral Fe site below the magnetic ordering temperature. The Kondo effect is, of course, usually studied in metals. Here, we show that it can also appear in a semiconductor that has both Mott and band gaps. Similar to the metallic Kondo effect, the orbitals with Mott-like gaps develop a many-body excitation near the valence edge. This draws the gap downward in energy (1.7 eV in $Zn_2Mo_3O_8$ $\rightarrow$ 1 eV in $Fe_2Mo_3O_8$) and screens the magnetic moment. This discovery opens the door to deeper exploration of the Kondo effect in semiconductors. $Fe_2Mo_3O_8$ is also a superb platform for unraveling structure-property relationships. What differentiates $Fe_2Mo_3O_8$ from the Zn, Mn, Co, and Ni members of this series is the band-Mott mixing, the Zhang-Rice resonance, and how the gap is hybridized. Taken together, these findings enhance our understanding of charge transfer in quantum cluster magnets and advance the use of this powerful scaffold in new types of charge storage devices.

ACKNOWLEDGMENTS

Research at the University of Tennessee and Rutgers University is supported by the NSF-DMREF program (Grants No. DMR-1629079 and No. DMR-1629059).

G.L.P.'s work was supported by a grant of the Romanian Ministry of Education and Research, CNCS - UEFISCDI, Project No. PN-III-P1-1.1-TE-2019-1767, within PNCDI III. Access to the x-ray facilities at the Research Complex, Rutherford Appleton Laboratory is gratefully acknowledged.

[1] S. V. Streltsov and D. I. Khomskii, Orbital physics in transition metal compounds: New trends, Phys. Usp. **60**, 1121 (2017).

[2] R. Morrow, R. Mishra, O. D. Restrepo, M. R. Ball, W. Windl, S. Wurmehl, U. Stockert, B. Büchner, and P. M. Woodward, Independent ordering of two interpenetrating magnetic sublattices in the double perovskite Sr_2CoOsO_6, J. Am. Chem. Soc. **135**, 18824 (2013).

[3] B. Yan, A. K. Paul, S. Kanungo, M. Reehuis, A. Hoser, D. M. Többens, W. Schnelle, R. C. Williams, T. Lancaster, F. Xiao, J. S. Möller, S. J. Blundell, W. Hayes, C. Felser, and M. Jansen, Lattice-Site-Specific Spin Dynamics in Double Perovskite Sr_2CoOsO_6, Phys. Rev. Lett. **112**, 147202 (2014).

[4] J. Gu, Y. Yan, J. W. Krizan, Q. D. Gibson, Z. M. Detweiler, R. J. Cava, and A. B. Bocarsly, *p*-type $CuRhO_2$ as a self-healing photoelectrode for water reduction under visible light, J. Am. Chem. Soc. **136**, 830 (2014).

[5] M. Ye, H.-S. Kim, J.-W. Kim, C.-J. Won, K. Haule, D. Vanderbilt, S.-W. Cheong, and G. Blumberg, Covalency-driven collapse of strong spin-orbit coupling in face-sharing iridium octahedra, Phys. Rev. B **98**, 201105 (2018).

[6] J. Singleton, J. W. Kim, C. V. Topping, A. Hansen, E.-D. Mun, S. Chikara, I. Lakis, S. Ghannadzadeh, P. Goddard, X. Luo, Y. S. Oh, S.-W. Cheong, and V. S. Zapf, Magnetic properties of Sr_3NiIrO_6 and Sr_3CoIrO_6: Magnetic hysteresis with coercive fields of up to 55 T, Phys. Rev. B **94**, 224408 (2016).

[7] K. R. O'Neal, A. Paul, A. Al-Wahish, K. D. Hughey, A. L. Blockmon, X. Luo, S.-W. Cheong, V. S. Zapf, C. V. Topping, J. Singleton, M. Ozerov, T. Birol, and J. L. Musfeldt, Spin-lattice and electron-phonon coupling in $3d/5d$ hybrid Sr_3NiIrO_6, npj Quantum Mater. **4**, 48 (2019).

[8] N. D. Khanh, N. Abe, H. Sagayama, A. Nakao, T. Hanashima, R. Kiyanagi, Y. Tokunaga, and T. Arima, Magnetoelectric coupling in the honeycomb antiferromagnet $Co_4Nb_2O_9$, Phys. Rev. B **93**, 075117 (2016).

[9] T. Liang, S. M. Koohpayeh, J. W. Krizan, T. M. McQueen, R. J. Cava, and N. P. Ong, Heat capacity peak at the quantum critical point of the transverse Ising magnet $CoNb_2O_6$, Nat. Commun. **6**, 7611 (2015).

[10] M. O. Yokosuk, H.-S. Kim, K. D. Hughey, J. Kim, A. V. Stier, K. R. O'Neal, J. Yang, S. A. Crooker, K. Haule, S.-W. Cheong, D. Vanderbilt, and J. L. Musfeldt, Nonreciprocal directional dichroism of a chiral magnet in the visible range, npj Quantum Mater. **5**, 20 (2020).

[11] D. Inosov, Quantum magnetism in minerals, Adv. Phys. **67**, 149 (2018).

[12] J. P. Sheckelton, J. R. Neilson, D. G. Soltan, and T. M. McQueen, Possible valence-bond condensation in the frustrated cluster magnet $LiZn_2Mo_3O_8$, Nat. Mater. **11**, 493 (2012).

[13] M. Mourigal, W. T. Fuhrman, J. P. Sheckelton, A. Wartelle, J. A. Rodriguez-Rivera, D. L. Abernathy, T. M. McQueen, and C. L. Broholm, Molecular Quantum Magnetism in $LiZn_2Mo_3O_8$, Phys. Rev. Lett. **112**, 027202 (2014).

[14] Y. Wang, G. L. Pascut, B. Gao, T. A. Tyson, K. Haule, V. Kiryukhin, and S.-W. Cheong, Unveiling hidden ferrimagnetism and giant magnetoelectricity in polar magnet $Fe_2Mo_3O_8$, Sci. Rep. **5**, 12268 (2015).

[15] T. Kurumaji, S. Ishiwata, and Y. Tokura, Doping-Tunable Ferrimagnetic Phase with Large Linear Magnetoelectric Effect in a Polar Magnet $Fe_2Mo_3O_8$, Phys. Rev. X **5**, 031034 (2015).

[16] Y. Li, G. Gao, and K. Yao, Dzyaloshinskii-Moriya interaction of polar magnet $Fe_2Mo_3O_8$ and its multiferroicity, Europhys. Lett. **118**, 37001 (2017).

[17] H. Chen, Magnetically driven orbital-selective insulator-metal transition in double perovskite oxides, npj Quantum Mater. **3**, 57 (2018).

[18] I. V. Solovyev and S. V. Streltsov, Microscopic toy model for magnetoelectric effect in polar $Fe_2Mo_3O_8$, Phys. Rev. Mater. **3**, 114402 (2019).

[19] S. A. Nikolaev, I. V. Solovyev, and S. V. Streltsov, Quantum spin liquid and cluster Mott insulator phases in the Mo_3O_8 magnets, npj Quantum Mater. **6**, 25 (2021).

[20] S. V. Streltsov, D. J. Huang, I. V. Solovyev, and D. I. Khomskii, Ordering of Fe and Zn ions and the magnetic properties of $FeZnMo_3O_8$, JETP Lett. **109**, 786 (2019).

[21] S. Nakayama, R. Nakamura, M. Akaki, D. Akahoshi, and H. Kuwahara, Ferromagnetic behavior of $(Fe_{1-y}Zn_y)_2Mo_3O_8$ ($0 \leqslant y \leqslant 1$) induced by nonmagnetic Zn substitution, J. Phys. Soc. Jpn. **80**, 104706 (2011).

[22] W. H. McCarroll, L. Katz, and R. Ward, Some ternary oxides of tetravalent molybdenum, J. Am. Chem. Soc. **79**, 5410 (1957).

[23] G. B. Ansell and L. Katz, A refinement of the crystal structure of zinc molybdenum(IV) oxide, $Zn_2Mo_3O_8$, Acta Crystallogr. **21**, 482 (1966).

[24] F. Varret, H. Czeskleba, F. Hartmann-Boutron, and P. Imbert, Study of the Mössbauer effect of the ion Fe^{2+} of trigonal symmetry in the compounds of the type $(Fe, M)_2Mo_3O_8$ (M = Mg, Zn, Mn, Co, Ni) and magnetic properties of $(Fe, Zn)_2Mo_3O_8$, J. Phys. **33**, 549 (1972).

[25] H. Czeskleba, P. Imbert, and F. Varret, Mössbauer study of $Fe_2Mo_3O_8$ and $FeZnMo_3O_8$, AIP Conf. Proc. **5**, 811 (1972).

[26] T. N. Stanislavchuk, G. L. Pascut, A. P. Litvinchuk, Z. Liu, S. Choi, M. J. Gutmann, B. Gao, K. Haule, V. Kiryukhin, S.-W. Cheong, and A. A. Sirenko, Spectroscopic and first principle DFT+eDMFT study of complex structural, electronic, and vibrational properties of $M_2Mo_3O_8$ (M = Fe, Mn) polar magnets, Phys. Rev. B **102**, 115139 (2020).

[27] S. Reschke, A. A. Tsirlin, N. Khan, L. Prodan, V. Tsurkan, I. Kézsmárki, and J. Deisenhofer, Structure, phonons, and orbital degrees of freedom in $Fe_2Mo_3O_8$, Phys. Rev. B **102**, 094307 (2020).

[28] M. G. Kim, H. Miao, B. Gao, S.-W. Cheong, C. Mazzoli, A. Barbour, W. Hu, S. B. Wilkins, I. K. Robinson, M. P. M. Dean, and V. Kiryukhin, Imaging antiferromagnetic antiphase domain boundaries using magnetic Bragg diffraction phase contrast, Nat. Commun. **9**, 5013 (2018).

[29] Y. S. Tang, J. H. Zhang, L. Lin, R. Chen, J. F. Wang, S. H. Zheng, C. Li, Y. Y. Zhang, G. Z. Zhou, L. Huang, Z. B. Yan, X. M. Lu, D. Wu, X. K. Huang, X. P. Jiang, and J.-M. Liu, Metamagnetic transitions and magnetoelectricity in the spin-1 honeycomb antiferromagnet $Ni_2Mo_3O_8$, Phys. Rev. B **103**, 014112 (2021).

[30] S. Yu, B. Gao, J. W. Kim, S.-W. Cheong, M. K. L. Man, J. Madéo, K. M. Dani, and D. Talbayev, High-Temperature Terahertz Optical Diode Effect without Magnetic Order in Polar $FeZnMo_3O_8$, Phys. Rev. Lett. **120**, 037601 (2018).

[31] B. Csizi, S. Reschke, A. Strinić, L. Prodan, V. Tsurkan, I. Kézsmárki, and J. Deisenhofer, Magnetic and vibronic terahertz excitations in Zn-doped $Fe_2Mo_3O_8$, Phys. Rev. B **102**, 174407 (2020).

[32] Y. M. Sheu, Y. M. Chang, C. P. Chang, Y. H. Li, K. R. Babu, G. Y. Guo, T. Kurumaji, and Y. Tokura, Picosecond Creation of Switchable Optomagnets from a Polar Antiferromagnet with Giant Photoinduced Kerr Rotations, Phys. Rev. X **9**, 031038 (2019).

[33] A. Biswas, H. Triki, Q. Zhou, S. P. Moshokoa, M. Z. Ullah, and M. Belic, Cubic-quartic optical solitons in Kerr and power law media, Optik **144**, 357 (2017).

[34] Q. Chen, A. Verrier, D. Ziat, A. J. Clune, R. Rouane, X. Bazier-Matte, G. Wang, S. Calder, K. M. Taddei, C. R. d. Cruz, A. I. Kolesnikov, J. Ma, J.-G. Cheng, Z. Liu, J. A. Quilliam, J. L. Musfeldt, H. D. Zhou, and A. A. Aczel, Realization of the orbital-selective Mott state at the molecular level in $Ba_3LaRu_2O_9$, Phys. Rev. Mater. **4**, 064409 (2020).

[35] G. L. Pascut and K. Haule, Role of orbital selectivity on crystal structures and electronic states in $BiMnO_3$ and $LaMnO_3$ perovskites, arXiv:2005.12179.

[36] A. I. Lichtenstein, M. I. Katsnelson, and G. Kotliar, Finite-Temperature Magnetism of Transition Metals: An *ab initio* Dynamical Mean-Field Theory, Phys. Rev. Lett. **87**, 067205 (2001).

[37] V. Anisimov, I. Nekrasov, D. Kondakov, T. Rice, and M. Sigrist, Orbital-selective Mott-insulator transition in $Ca_{2-x}Sr_xRuO_4$, Eur. Phys. J. B **25**, 191 (2002).

[38] L. de'Medici, A. Georges, and S. Biermann, Orbital-selective Mott transition in multiband systems: Slave-spin representation and dynamical mean-field theory, Phys. Rev. B **72**, 205124 (2005).

[39] K. Haule and G. L. Pascut, Mott transition and magnetism in rare earth nickelates and its fingerprint on the x-ray scattering, Sci. Rep. **7**, 10375 (2017).

[40] P. Blaha, K. Schwarz, G. Madsen, D. Kvasnicka, J. Luitz, R. Laskowsk, F. Tran, L. Marks, and L. Marks, *WIEN2k: An Augmented Plane Wave Plus Local Orbitals Program for Calculating Crystal Properties* (Techn. Universitat, Rutgers University, 2019).

[41] K. Haule, DMFT code (2007–2020), http://hauleweb.rutgers.edu/tutorials/ (unpublished).

[42] K. Haule, Structural predictions for correlated electron materials using the functional dynamical mean field theory approach, J. Phys. Soc. Jpn. **87**, 041005 (2018).

[43] J. P. Perdew, K. Burke, and M. Ernzerhof, Generalized Gradient Approximation Made Simple, Phys. Rev. Lett. **77**, 3865 (1996).

[44] K. Haule, Exact Double Counting In Combining The Dynamical Mean Field Theory and the Density Functional Theory, Phys. Rev. Lett. **115**, 196403 (2015).

[45] K. Haule, Quantum Monte Carlo impurity solver for cluster dynamical mean-field theory and electronic structure calculations with adjustable cluster base, Phys. Rev. B **75**, 155113 (2007).

[46] K. Haule, DFT + embedded DMFT functional, http://hauleweb.rutgers.edu/tutorials/ (unpublished).

[47] See Supplemental Material at http://link.aps.org/supplemental/10.1103/PhysRevB.104.195143.doi for additional details about experimental and theoretical analysis on d-to-d excitations, charge gap, vibronic coupling, electronic structure calculations, and many-body effect.

[48] J. I. Pankove, *Optical Processes in Semiconductors*, 2nd ed. (Dover, New York, 2010).

[49] C. Ballhausen, *Introduction to Ligand Field Theory*, McGraw-Hill Series in Advanced Chemistry (McGraw-Hill, New York, 1962).

[50] A. Stoneham, *Theory of Defects in Solids: Electronic Structure of Defects in Insulators and Semiconductors*, Oxford Classic Texts in the Physical Sciences (Clarendon Press, Oxford, 2001).

[51] K. R. O'Neal, A. Al-Wahish, Z. Li, P. Chen, J. W. Kim, S. W. Cheong, G. Dhalenne, A. Revcolevschi, X. T. Chen, and J. L. Musfeldt, Vibronic coupling and band gap trends in $CuGeO_3$ nanorods, Phys. Rev. B **96**, 075437 (2017).

[52] J. W. Evans, T. R. Harris, B. R. Reddy, K. L. Schepler, and P. A. Berry, Optical spectroscopy and modeling of Fe^{2+} ions in zinc selenide, J. Lumin. **188**, 541 (2017).

[53] P. K. Sarswat and M. L. Free, A study of energy band gap versus temperature for Cu_2ZnSnS_4 thin films, Phys. B: Condens. Matter **407**, 108 (2012).

[54] K. P. O'Donnell and X. Chen, Temperature dependence of semiconductor band gaps, Appl. Phys. Lett. **58**, 2924 (1991).

[55] C.-H. Yee, G. Kotliar, and K. Haule, Valence fluctuations and quasiparticle multiplets in plutonium chalcogenides and pnictides, Phys. Rev. B **81**, 035105 (2010).

[56] A. C. Hewson, *The Kondo Problem to Heavy Fermions* (Cambridge University Press, Cambridge, 1993).

[57] S. Mandal, K. Haule, K. M. Rabe, and D. Vanderbilt, Systematic beyond-DFT study of binary transition metal oxides, npj Comput. Mater. **5**, 115 (2019).

[58] S. Mandal, K. Haule, K. M. Rabe, and D. Vanderbilt, Influence of magnetic ordering on the spectral properties of binary transition metal oxides, Phys. Rev. B **100**, 245109 (2019).

[59] F. C. Zhang and T. M. Rice, Effective Hamiltonian for the superconducting Cu oxides, Phys. Rev. B **37**, 3759 (1988).

[60] H. Eskes and G. A. Sawatzky, Tendency Towards Local Spin Compensation of Holes in the High-T_c Copper Compounds, Phys. Rev. Lett. **61**, 1415 (1988).

[61] *The Physics of Correlated Insulators, Metals, and Superconductors*, edited by E. Pavarini, E. Koch, R. Scalettar, and R. Martin, Schriften des Forschungszentrums Jülich Reihe Modeling and Simulation, Vol. 7 (Forschungszentrum Jülich GmbH Zentralbibliothek, Verlag, Jülich, 2017), p. 450.

[62] D. O. Demchenko, A. V. Joura, and J. K. Freericks, Effect of Particle-Hole Asymmetry on the Mott-Hubbard Metal-Insulator Transition, Phys. Rev. Lett. **92**, 216401 (2004).

[63] G. Kotliar, S. Y. Savrasov, K. Haule, V. S. Oudovenko, O. Parcollet, and C. A. Marianetti, Electronic structure calculations with dynamical mean-field theory, Rev. Mod. Phys. **78**, 865 (2006).